

# Metallic molybdenum disulfide nanosheet-based electrochemical actuators

Muharrem Acerce<sup>1</sup>, E. Koray Akdoğan<sup>1</sup> & Manish Chhowalla<sup>1</sup>

**Actuators that convert electrical energy to mechanical energy are useful in a wide variety of electromechanical systems and in robotics<sup>1–6</sup>, with applications such as steerable catheters<sup>7</sup>, adaptive wings for aircraft and drag-reducing wind turbines<sup>8</sup>. Actuation systems can be based on various stimuli, such as heat, solvent adsorption/desorption<sup>4,9</sup>, or electrochemical action (in systems such as carbon nanotube electrodes<sup>1,10</sup>, graphite electrodes<sup>11</sup>, polymer electrodes<sup>6,12–14</sup> and metals<sup>15</sup>). Here we demonstrate that the dynamic expansion and contraction of electrode films formed by restacking chemically exfoliated nanosheets of two-dimensional metallic molybdenum disulfide (MoS<sub>2</sub>) on thin plastic substrates can generate substantial mechanical forces. These films are capable of lifting masses that are more than 150 times that of the electrode over several millimetres and for hundreds of cycles. Specifically, the MoS<sub>2</sub> films are able to generate mechanical stresses of about 17 megapascals—higher than mammalian muscle (about 0.3 megapascals)<sup>3</sup> and comparable to ceramic piezoelectric actuators (about 40 megapascals)—and strains of about 0.6 per cent, operating at frequencies up to 1 hertz. The actuation performance is attributed to the high electrical conductivity of the metallic 1T phase of MoS<sub>2</sub> nanosheets, the elastic modulus of restacked MoS<sub>2</sub> layers (2 to 4 gigapascals) and fast proton diffusion between the nanosheets. These results could lead to new electrochemical actuators for high-strain and high-frequency applications.**

Electroactive polymers have been studied for actuation applications over the past few decades, but the stress generation ability of polymers has remained low, generally because of their low Young's modulus, though mechanical performance as well as work density at low rates can be increased by incorporating carbon nanotubes into conjugated polymers<sup>16</sup>. Recent studies of Au-Pt nanoporous metal actuators have revealed exceptionally high strains<sup>15</sup>, but such high strains were achieved at relatively low frequencies (0.00025 Hz) and such actuator materials are expensive. The use of abundant materials such as metallic NiOOH and V<sub>2</sub>O<sub>5</sub> fibres can mitigate the cost of metallic actuators<sup>17,18</sup>, though the performance of these particular actuators depends on the crystallographic orientation of the material. See Extended Data Table 1 for a literature survey of actuator performance.

In this study, we report a macroscopic actuation device, the mechanism of which is the electrochemically induced insertion and removal of cations between two-dimensional (2D) nanosheets of 1T MoS<sub>2</sub> (see Extended Data Fig. 1; applied voltage from +0.3 V to −0.3 V is required for removal and insertion of cations). Two-dimensional materials such as MoS<sub>2</sub> nanosheets have high surface to volume ratios, enabling large amounts of electrochemical charge storage. The stored electrochemical charge—which affects the interatomic bonds and the distance between atoms via double-layer formation<sup>1,19</sup>, ion intercalation<sup>11</sup> or Faradaic reaction<sup>17</sup>—reconfigures the space-charge region in the vicinity of the electrode–electrolyte interface. The use of this sort of intercalation mechanism to induce expansion has previously been demonstrated in graphite battery electrodes; under a pre-stress loading of 10 MPa, strain and energy density values of 6.7% and 670 kJ m<sup>−3</sup>, respectively, were

achieved in electrochemical cells comprising LiCoO<sub>2</sub> cathodes and bulk micromachined highly oriented pyrolytic graphite anodes. Expansion occurred because of synergistic expansion of both the cathode and the anode during delithiation and lithiation, respectively<sup>11</sup>, giving an energy density of 1.3 MJ m<sup>−3</sup> and strain values of 1.8% under 100 MPa applied load, along with strains of 1% at frequencies of 6.7 MHz under 2 MPa loading in a fully packaged 740 mA h packaged Li-ion battery. However, the expansion of the electrodes occurred at high voltages (3.0–4.5 V), and while this expansion could be used for actuation, no working actuator was reported. Following up this work, it was demonstrated<sup>20</sup> that expansion of graphite electrodes can lead to strains of up to 3% at zero stress values and 1% at 5 MPa, with an operation frequency of 10 MHz.

The actuation that we report with metallic MoS<sub>2</sub> films that are formed by restacking chemically exfoliated nanosheets is fully reversible and highly stable over a broad frequency range that can be controlled with potential and scan rate (see Fig. 1 and Extended Data Figs 2, 3). The reversible bending in both directions of a Kapton beam coated with 1T MoS<sub>2</sub> nanosheets, shown in Fig. 1 (and Supplementary Videos 1 and 2), is attributed to the strain induced by expansion and contraction of the MoS<sub>2</sub> film. The actuation can be explained by assuming quasi-static conditions in which the elastic strain represents the change in length due to expansion or contraction of the MoS<sub>2</sub> film.

Briefly, the actuator comprises of an electrochemically active film (1T MoS<sub>2</sub>) that is deposited on a much thicker substrate (the Kapton beam in this case). The whole device is immersed in H<sub>2</sub>SO<sub>4</sub> electrolyte. Therefore, the state of stress in the 1T MoS<sub>2</sub> film is plane stress. In other words, the out-of-plane stress is zero because there are no traction forces on a free surface, that is,  $\sigma_{\perp} = 0$ , while the in-plane stress is not zero because of the traction forces at the film–substrate interface, that is,  $\sigma_{\parallel} \neq 0$ . Here, we have in-plane isotropy and all shear stresses vanish since the 1T MoS<sub>2</sub> nanosheets are randomly oriented in the plane of the film. However, none of the normal strains are zero, that is,  $\varepsilon_{\perp} \neq 0$  and  $\varepsilon_{\parallel} \neq 0$ . Under plane stress conditions,  $\varepsilon_{\perp}$  and  $\varepsilon_{\parallel}$  are related by  $\varepsilon_{\perp} = -2(E_{\parallel}/E_{\perp})\varepsilon_{\parallel}$ , where  $E_{\parallel}$  and  $E_{\perp}$  are the in-plane and out-of-plane elastic moduli, respectively. In this study, we obtained the  $E_{\perp}$  by nanoindentation (see Extended Data Fig. 4), while  $E_{\parallel}$  was obtained from the curvature data in conjunction with the beam theory model (see Extended Data Fig. 5 and Methods). In materials physics, the elastic compliance  $S_{ij}$  ( $i, j$  range from 1 to 6) is the reciprocal tensor element of the corresponding modulus of elasticity  $E_{ij}$  so that  $E_{ij} = 1/S_{ij}$ . Hence, Poisson's ratio is related to the appropriate longitudinal and transverse moduli of elasticity based on first principles, but is expressed as the ratio of transverse strain to longitudinal strain. In our case, the ratio  $(\varepsilon_{\parallel}/\varepsilon_{\perp})$  is the approximate Poisson's ratio of the 2D MoS<sub>2</sub> nanosheets, which has been established to be about 0.3 (ref. 21).

When the actuator is immersed in the electrolyte, the intercalating species diffuse into the 1T MoS<sub>2</sub> film through all surfaces that are in contact with the solution. The intercalation causes charge screening between the 1T MoS<sub>2</sub> sheets, affecting the bond strengths and thereby the inter-sheet separation. The film contracts in the out-of-plane

<sup>1</sup>Materials Science and Engineering, Rutgers University, 607 Taylor Road, Piscataway, New Jersey, USA.

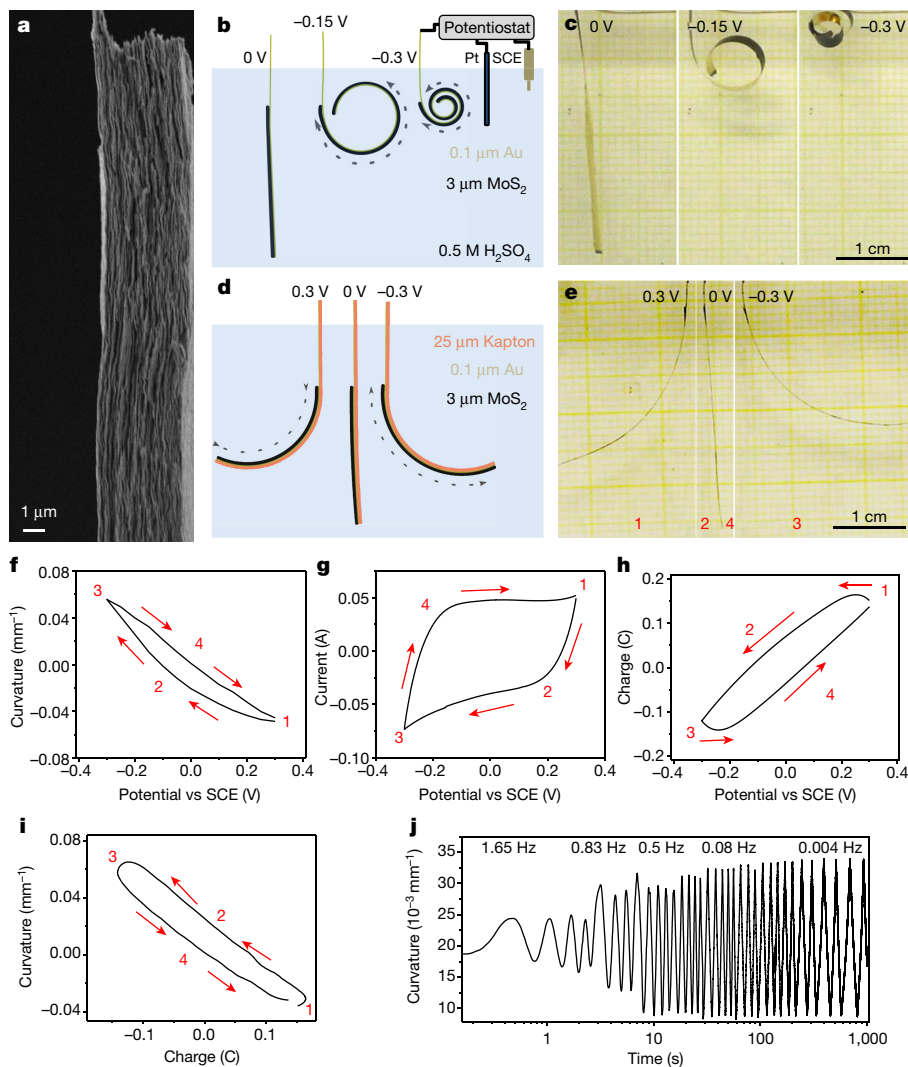


**Figure 1 | Experimental set-up for actuation measurements.** **a**, Scanning electron microscope image of restacked 1T phase 2D MoS<sub>2</sub> film. **b**, The electrochemical system consists of a working electrode (the actuator) along with a counter electrode (Pt) and a reference electrode (standard calomel electrode, SCE) submerged in 0.5 M H<sub>2</sub>SO<sub>4</sub>. **c**, Images of curvature induced by charge intercalation in free-standing (that is, no Kapton beam) 1T MoS<sub>2</sub> film on gold (scale bar, 1 cm). **d**, **e**, Diagram (**d**) and photograph (**e**) of actuation in forward and backward directions by modulation of the electrode potential between  $-0.3$  V and  $+0.3$  V. The numbers correspond

direction; that is, the out-of-plane strain is compressive ( $\varepsilon_{\perp} < 0$ ), because the positively charged intercalating species pull the negatively charged nanosheets closer together. A similar phenomenon has been demonstrated and confirmed by *in situ* X-ray diffraction (XRD) measurements in other two-dimensional nanosheets<sup>22</sup>. The contraction, which is perpendicular to the normal surface of the film, is accompanied by an expansion in the plane of the coating, that is,  $\varepsilon_{\parallel} > 0$ . Owing to the traction forces at the 1T MoS<sub>2</sub> film–substrate interface and the geometry of the actuator, the tensile in-plane strain ( $\varepsilon_{\parallel} > 0$ ) causes a torque around the base of the actuator, resulting in a net upward displacement that is proportional with the extent of intercalation (ultimately reaching saturation). The high charge storage capacity of 1T MoS<sub>2</sub> accommodates larger amounts of ion flux into the film, resulting in higher electrochemical actuation behaviour. We found a linear relationship between actuation and potential window (Extended Data Fig. 3).

Our previous *ex situ* XRD studies<sup>23</sup> showed that during negative potential sweeps, cations are intercalated between—and are also adsorbed onto—the MoS<sub>2</sub> nanosheets. During positive potential

to the Kapton beam position as shown in **d**. Charging of the film (position 1) induces curvature of the Kapton beam to the left due to volume expansion from intercalation. Position 3 corresponds to the contraction of the film due to discharge, leading to curvature in the opposite direction. **f**, Curvature versus potential data from charging and discharging of 1T phase 2D MoS<sub>2</sub> film. **g**, **h**, Current (**g**) and charge (**h**) versus the applied potential. **i**, Curvature due to charge intercalation. **j**, Actuation at different cycling frequencies, demonstrating actuation over a range of frequencies.

sweeps, protons are removed from the MoS<sub>2</sub> film. The amount of ion movement can be calculated from the measured current and the corresponding curvature change can be correlated with it. The curvature change and the amount of charge flow changes linearly with respect to the applied potential, as shown in Fig. 1h–j. The curvature change and specific capacitance decrease slightly with increasing frequency, as shown in Extended Data Fig. 2c. The curvature also varies linearly with specific capacitance (Extended Data Fig. 2d). The actuation can thus be explained by the high conductivity of the 1T phase as well as high ionic diffusivity in restacked MoS<sub>2</sub> nanosheets due to large anionic polarizability<sup>24</sup>. These phenomena enable high actuation performance even at high frequencies, compared to other electroactive materials governed by pseudocapacitive<sup>17,18</sup> or adsorbate-induced actuation<sup>5,19</sup>.

Mechanical models<sup>25</sup> for multilayer actuators provide useful methods for calculating the elongation (approximated as the effective strain) and elastic modulus of the actuator material (see Methods for a detailed derivation). According to beam bending theory, the induced strain is related to the observed curvature  $\kappa$  by  $\kappa = 1/R = c_{\perp}\varepsilon$ , where  $R$  is the

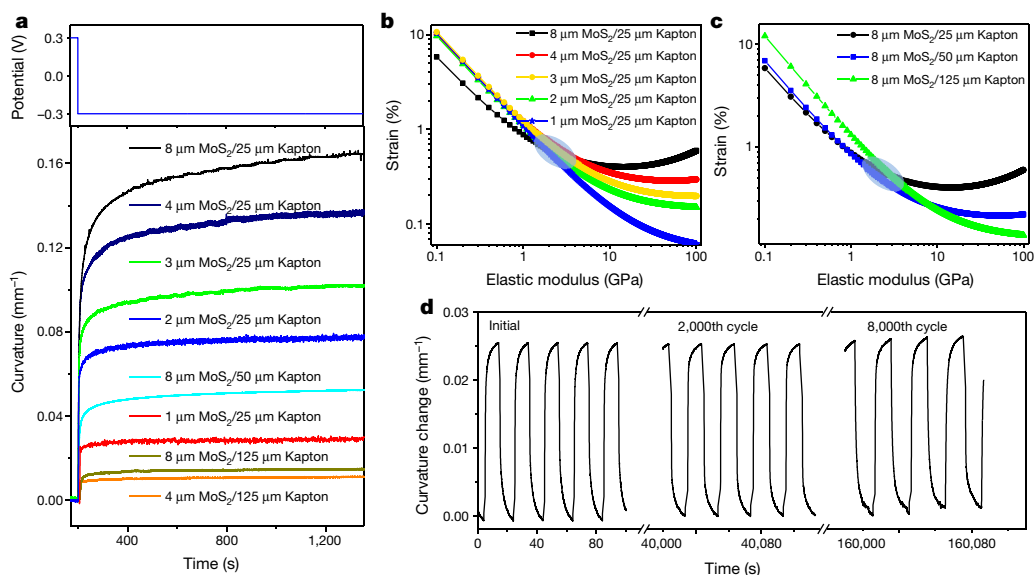


**Figure 2 | Measurements of strain and in-plane modulus using the beam bending model.** **a**, Bottom panel, curvature of Kapton beams of different thicknesses induced by 1T phase 2D MoS<sub>2</sub> nanosheet electrodes of different thicknesses. Top panel, the potential profile used for charging. **b**, Calculated values of strain versus elastic modulus for 25- $\mu\text{m}$  Kapton beams and different thicknesses of MoS<sub>2</sub> films. **c**, Calculated strain versus elastic modulus values for constant MoS<sub>2</sub> film thickness and variable thickness of Kapton beam. The shaded regions shown in **b** and **c** are

cross-over points that give values of strain and elastic modulus of the MoS<sub>2</sub> film. The strain can be seen to range from 0.4% to 0.8%, and the in-plane modulus varies from 2 GPa to 4 GPa. The uncertainty in strain based on thickness and elastic modulus using nanoindentation variations is approximately 10%. **d**, Cycling stability of MoS<sub>2</sub>-coated Kapton bimorph. The bimorph exhibited stable continuous actuation for the three days it was tested.

radius of curvature,  $\varepsilon$  is the strain and  $c_k$  is dependent on the elastic moduli and thicknesses of the actuating layer and the beam. By changing the thicknesses of the MoS<sub>2</sub> film and of the beam, it is possible to obtain specific  $c_k$  coefficients. The thicknesses and elastic modulus of the polyimide (Kapton) beam are known, but the modulus of restacked MoS<sub>2</sub> nanosheets has not been experimentally measured.

However, by measuring the curvature of Kapton beams of different thicknesses with MoS<sub>2</sub> film electrodes of different thicknesses as shown in Fig. 2a, it is possible to plot the effective strain as a function of elastic modulus (Fig. 2b, c). By assuming that the effective strain and elastic modulus of the MoS<sub>2</sub> do not change with the thickness of the film (as supported by our nanoindentation results that yield almost identical

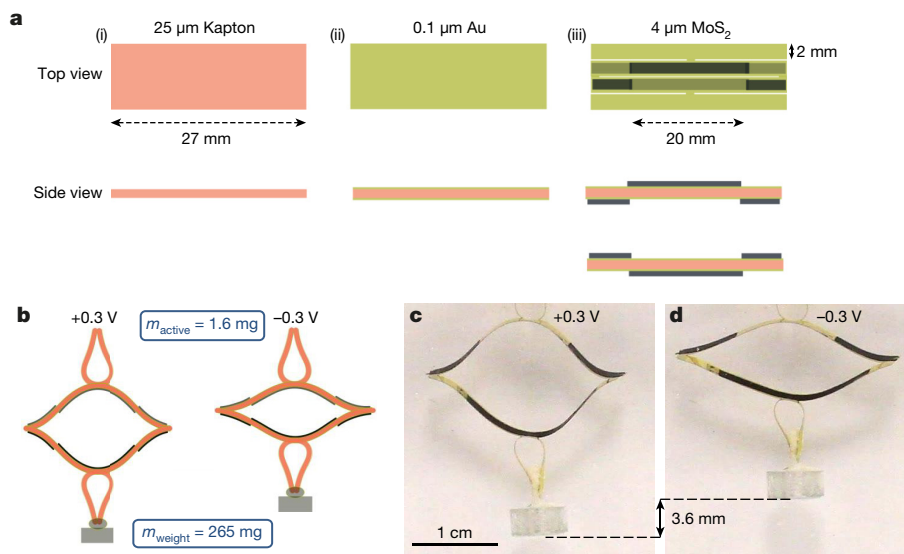


**Figure 3 | Inverted-series-connected (ISC) bimorph actuation device based on metallic MoS<sub>2</sub> nanosheet electrodes.** **a**, Diagram of ISC actuator fabrication. First, a 100-nm gold layer (shown green) was deposited on both sides of 25- $\mu\text{m}$  Kapton tape (shown pink; i, ii). The gold-coated Kapton film was then cut into four strips as illustrated to form interconnected gold electrode strips of dimension 2 mm  $\times$  25 mm. After this, 4- $\mu\text{m}$  MoS<sub>2</sub> film (shown dark green) was transferred on the designated areas on both sides of the strips (iii). Then the strips are rotated by 180° degrees in the plane of their surface, and the strips are then joined at the ends. **b**, Diagrams of the assembled ISC bimorph actuator with a

265-mg weight attached. The black regions in the schematic represent the locations of the MoS<sub>2</sub> film on the assembled device. Left panel, at the equilibrium position at an open circuit voltage of +0.3 V; right panel, showing the lifting of the weight via the application of -0.3 V. **c**, **d**, Photographs of the actuator at the equilibrium position (**c**) and upon charging of the film, which leads to lifting of the weight by 3.6 mm (**d**). The measurements were done immersed in 0.5 M H<sub>2</sub>SO<sub>4</sub> electrolyte. Supplementary Video 3 shows the actuation motion of the ISC bimorph device.

moduli values for the 3- $\mu\text{m}$  and 8- $\mu\text{m}$  films)—that is, there are no gradients in composition on intercalation—we postulate that the point at which the curves in Fig. 2b and c cross represents the real values of the effective strain and elastic modulus. It can be seen that the restacked 2D 1T MoS<sub>2</sub> nanosheets have  $E_{\parallel}$  values ranging from 2 GPa to 4 GPa and strain values of up to 0.8% (or average values of  $0.6\% \pm 0.2\%$ ). On the basis of these measurements and following Hooke's law, the strength of the material is estimated to be approximately 17 MPa. This stress, from charge-induced deformation of 1T MoS<sub>2</sub>, is much larger than that from mammalian muscle (0.3 MPa) and is comparable to that from piezoelectric materials (40 MPa). In addition, the actuation is stable for up to three days, as shown in Fig. 2d.

To substantiate our model, we used nanoindentation to measure the modulus of 1T MoS<sub>2</sub> films in the charged, discharged and dry states. We found that the modulus of the film changes during charging and discharging, as also found in other 2D materials<sup>26</sup>. It should be noted that the elastic modulus obtained by nanoindentation is the out-of-plane modulus designated  $E_{\perp}$ , which is very approximately related to the in-plane modulus  $E_{\parallel}$  via Poisson's ratio ( $\nu$ ) as  $E_{\parallel} \approx \nu E_{\perp}$ . For MoS<sub>2</sub>, Poisson's ratio is well established as  $\nu \approx 0.3$  (ref. 21). Taking  $E_{\perp} = 8.4$  GPa found from nanoindentation of the charged film, we obtain  $E_{\parallel} \approx 2.5 \pm 0.1$  GPa, which is in agreement with recent tensile test results<sup>27</sup> and with what our model predicts for  $E_{\parallel}$  on the basis of beam bending mechanics.

The performance of electrochemical actuators is characterized by the work density per cycle that is generally determined by the product of the elastic modulus and the square of the strain: that is,  $E\varepsilon_{\text{max}}^2/2$ . Using this relationship, the work density for freely actuated MoS<sub>2</sub> films—that is, without being attached to a Kapton substrate—is calculated as  $46 \text{ kJ m}^{-3}$  and  $81 \text{ kJ m}^{-3}$  for strains of 0.6% and 0.8%, respectively. To investigate whether the actuation properties of 1T MoS<sub>2</sub> can be translated into a working device, we designed an inverted-series-connected (ISC) bimorph actuator<sup>28,29</sup> shown in Fig. 3 (also see Extended Data Fig. 6). ISC bimorph actuators consist of two bimorph beams attached end to end, and in which active actuator films are applied to opposite sides of the beams, as shown in Fig. 3a and b. This enables each bimorph actuator to curve with an equal magnitude to cancel out the rotational angle of each, so that pure vertical displacement can occur. In other words, the ISC configuration enables one to amplify the axial displacement by taking advantage of deformation geometry, which in turn is controlled by the shape of the actuator. With this configuration, under fixed load, the ISC actuator behaves like an elliptical spring and is considered as a single-piece, passive compliant actuator with no moving parts<sup>30</sup>. We applied 4- $\mu\text{m}$ -thick films of 2D 1T MoS<sub>2</sub> to each beam (total film weight 1.6 mg). To demonstrate vertical lifting, we suspended a 265 mg weight from the ISC bimorph actuator, and initiated charging and discharging cycles.

It can be seen from the images in Fig. 3c and from Supplementary Video 3 that the 1T MoS<sub>2</sub> actuator is able to lift more than 150 times its own weight. We measured hundreds of cycles and found that the actuation remained stable. The energy density of the ISC bimorph actuator, as obtained by taking gravitational, buoyancy, spring and friction forces into account was found to be approximately  $6 \text{ kJ m}^{-3}$ . The work density could be increased further by judiciously increasing the MoS<sub>2</sub> layer thickness, decreasing the thickness of the Kapton layer, or using a more compliant substrate<sup>25</sup>.

**Online Content** Methods, along with any additional Extended Data display items and Source Data, are available in the online version of the paper; references unique to these sections appear only in the online paper.

**Received 10 January; accepted 21 July 2017.**

**Published online 30 August 2017.**

- Baughman, R. H. Carbon nanotube actuators. *Science* **284**, 1340–1344 (1999).
- Zhang, Q. M. Giant electrostriction and relaxor ferroelectric behavior in electron-irradiated poly(vinylidene fluoride-trifluoroethylene) copolymer. *Science* **280**, 2101–2104 (1998).

- Brochu, P. & Pei, Q. Advances in dielectric elastomers for actuators and artificial muscles. *Macromol. Rapid Commun.* **31**, 10–36 (2010).
- Aliev, A. E. *et al.* Giant-stroke, superelastic carbon nanotube aerogel muscles. *Science* **323**, 1575–1578 (2009).
- Biener, J. *et al.* Surface-chemistry-driven actuation in nanoporous gold. *Nat. Mater.* **8**, 47–51 (2009).
- Bar-Cohen, Y. (ed.) *Electroactive Polymer (EAP) Actuators as Artificial Muscles: Reality, Potential, and Challenges* 2nd edn (SPIE, 2004).
- Mazzoldi, A. & De Rossi, D. Conductive-polymer-based structures for a steerable catheter. *Proc. SPIE* **3987**, 273 (2000).
- Barbarino, S., Bilgen, O., Ajaj, R. M., Friswell, M. I. & Inman, D. J. A review of morphing aircraft. *J. Intell. Mater. Syst. Struct.* **22**, 823–877 (2011).
- Ma, M., Guo, L., Anderson, D. G. & Langer, R. Bio-inspired polymer composite actuator and generator driven by water gradients. *Science* **339**, 186–189 (2013).
- Yun, Y. *et al.* A multi-wall carbon nanotube tower electrochemical actuator. *Nano Lett.* **6**, 689–693 (2006).
- Koyama, Y. *et al.* Harnessing the actuation potential of solid-state intercalation compounds. *Adv. Funct. Mater.* **16**, 492–498 (2006).
- Lu, W. Use of ionic liquids for  $\pi$ -conjugated polymer electrochemical devices. *Science* **297**, 983–987 (2002).
- Pei, Q. & Inganaes, O. Electrochemical applications of the bending beam method. 1. Mass transport and volume changes in polypyrrole during redox. *J. Phys. Chem.* **96**, 10507–10514 (1992).
- Shahinpoor, M., Bar-Cohen, Y., Simpson, J. O. & Smith, J. Ionic polymer-metal composites (IPMCs) as biomimetic sensors, actuators and artificial muscles — a review. *Smart Mater. Struct.* **7**, R15–R30 (1998).
- Jin, H.-J. *et al.* Nanoporous Au–Pt alloys as large strain electrochemical actuators. *Nano Lett.* **10**, 187–194 (2010).
- Spinks, G. M., Mottaghtalab, V., Bahrami-Samani, M., Whitten, P. G. & Wallace, G. G. Carbon-nanotube-reinforced polyaniline fibers for high-strength artificial muscles. *Adv. Mater.* **18**, 637–640 (2006).
- Cheng, C. & Ngan, A. H. W. Reversible electrochemical actuation of metallic nanohoneycombs induced by pseudocapacitive redox processes. *ACS Nano* **9**, 3984–3995 (2015).
- Gu, G. *et al.* V<sub>2</sub>O<sub>5</sub> nanofibre sheet actuators. *Nat. Mater.* **2**, 316–319 (2003).
- Weissmuller, J. Charge-induced reversible strain in a metal. *Science* **300**, 312–315 (2003).
- Chin, T. E., Rhyner, U., Koyama, Y., Hall, S. R. & Chiang, Y.-M. Lithium rechargeable batteries as electromechanical actuators. *Electrochem. Solid-State Lett.* **9**, A134 (2006).
- Cooper, R. C. *et al.* Nonlinear elastic behavior of two-dimensional molybdenum disulfide. *Phys. Rev. B* **87**, 035423 (2013).
- Come, J. *et al.* Controlling the actuation properties of MXene paper electrodes upon cation intercalation. *Nano Energy* **17**, 27–35 (2015).
- Acerce, M., Voiry, D. & Chhowalla, M. Metallic 1T phase MoS<sub>2</sub> nanosheets as supercapacitor electrode materials. *Nat. Nanotechnol.* **10**, 313–318 (2015).
- Feng, P., Bu, X. & Zheng, N. The interface chemistry between chalcogenide clusters and open framework chalcogenides. *Acc. Chem. Res.* **38**, 293–303 (2005).
- Du, P., Lin, X. & Zhang, X. A multilayer bending model for conducting polymer actuators. *Sens. Actuators Phys.* **163**, 240–246 (2010).
- Come, J. *et al.* Nanoscale elastic changes in 2D Ti<sub>3</sub>C<sub>2</sub>T<sub>x</sub> (MXene) pseudocapacitive electrodes. *Adv. Energy Mater.* **6**, 1502290 (2016).
- Ge, Y. *et al.* A robust free-standing MoS<sub>2</sub>/poly(3,4-ethylenedioxythiophene): poly(styrenesulfonate) film for supercapacitor applications. *Electrochim. Acta* **235**, 348–355 (2017).
- Jia, K., Pal, S. & Xie, H. An electrothermal tip-tilt-piston micromirror based on folded dual S-shaped bimorphs. *J. Microelectromech. Syst.* **18**, 1004–1015 (2009).
- Otero, T. F., Cortes, M. T. & Boyano, I. Macroscopic devices and complex movements developed with artificial muscles. *Proc. SPIE* **4695**, 395–402 (2002).
- Ham, R., Sugar, T., Vanderborcht, B., Hollander, K. & Lefeber, D. Compliant actuator designs. *IEEE Robot. Autom. Mag.* **16**, 81–94 (2009).

**Supplementary Information** is available in the online version of the paper.

**Acknowledgements** M.A. acknowledges the Turkish Ministry of Education for a graduate fellowship. M.C. acknowledges support from NSF grant ECCS 1128335. E.K.A. acknowledges support from Rutgers MSE Department.

**Author Contributions** M.C. and M.A. conceived the idea and designed the experiments. M.A. synthesized the materials, carried out the electrochemical measurements, performed bending beam analyses and assisted E.K.A. with beam bending models. M.C. wrote the manuscript with assistance from M.A. and E.K.A. All authors discussed the results and commented on the manuscript.

**Author Information** Reprints and permissions information is available at [www.nature.com/reprints](http://www.nature.com/reprints). The authors declare no competing financial interests. Readers are welcome to comment on the online version of the paper. Publisher's note: Springer Nature remains neutral with regard to jurisdictional claims in published maps and institutional affiliations. Correspondence and requests for materials should be addressed to M.C. ([manish1@soe.rutgers.edu](mailto:manish1@soe.rutgers.edu)).

## METHODS

**MoS<sub>2</sub> thin film preparation.** Chemically exfoliated monolayer MoS<sub>2</sub> was synthesized by organo-lithium chemistry. Lithium intercalation into bulk MoS<sub>2</sub> powder was followed by exfoliation in deionized water as previously reported<sup>31</sup>. Briefly, 4 ml butyl-lithium and 20 ml hexane were added to 0.4 g of bulk MoS<sub>2</sub> powder under argon, and then heated up at reflux for 3 days. The mixture was cooled and then filtered with extra hexane (5 × 25 ml) to remove the excess of lithium and organic residues. The lithiated MoS<sub>2</sub> powder (Li<sub>x</sub>MoS<sub>2</sub>) was then mixed with deionized water at a ratio of 1.5 mg per ml and subsequently exfoliated. The solution was sonicated for 1 h to agitate the exfoliation, and centrifuged several times to remove lithium cations as well as the non-exfoliated materials.

Thin films were prepared by filtering the suspended chemically exfoliated single-layer MoS<sub>2</sub> nanosheets over nitrocellulose membranes (Millipore, 25 nm pore size) and then transferred onto a substrate (25 μm, 50 μm or 125 μm polyimide) that had been coated with a 100-nm gold layer. The thickness of the restacked 1T MoS<sub>2</sub> film was controlled by the volume of the MoS<sub>2</sub> solution. The thicknesses were measured by cross-sectional scanning electron microscopy. We made 100 measurements per sample and found them to be: 1 ± 0.1 μm, 2 ± 0.2 μm, 3 ± 0.1 μm, 4 ± 0.1 μm and 8 ± 0.2 μm. These thickness values were used for various devices and measurements described above. Finally, the membrane was dissolved in acetone and the restacked MoS<sub>2</sub> was dried in vacuum for a week. For the bilayer film (MoS<sub>2</sub>/gold), a sacrificial layer of PMMA was coated onto the substrate before gold deposition, and was dissolved in acetone.

**Actuation measurements.** To track the displacement and bending curvature, one end of the actuator was clamped as a working electrode and the other end was dipped vertically in a rectangular glass container filled with the electrolyte, 0.5 M H<sub>2</sub>SO<sub>4</sub>. Then, the actuator electrodes were electrochemically induced by applying a triangular or square wave potential (−0.3 V to 0.3 V) with respect to a calomel reference electrode in a three-electrode configuration via a Multistat (Solartron 1470). The free end displacement and the resolved bending degree of the actuator were recorded by a charge coupled device (Canon 60D) as shown in Fig. 1. The change in the electrode curvature produced as an electrochemical response was recorded with a resolution of 0.0001 mm<sup>−1</sup>.

**Chemicals and reagents.** Bulk MoS<sub>2</sub> powder was purchased from Alfa Aesar. *n*-butyllithium (1.6 M in hexane) and sulfuric acid (98%) was purchased from Sigma Aldrich and used as received. Kapton film was purchased from Dupont.

**Physical characterization.** Scanning electron microscope (SEM) images were obtained with a Zeiss Sigma Field Emission SEM with an Oxford INCA PentaFETx3 EDS system (Model 8100). X-ray photoelectron spectroscopy (XPS) measurements were performed with a Thermo Scientific K-Alpha spectrometer. All spectra were taken using an Al Kα microfocused and monochromatized source (1,486.7 eV) having a resolution of 0.6 eV, and a spot size of 400 μm. Raman spectral analyses were carried out using a Renishaw inVia system, operating at 514 nm (2.41 eV). X-ray diffraction (XRD) experiments were performed with a PANalytical X-ray diffractometer (model PW3040/60) using a Cu Kα radiation source (λ = 1.5418 Å).

**Electrochemical and actuation measurements.** Electrochemical measurements were conducted using a Solartron Multistat 1470 with a three-electrode cell configuration in 0.5 M H<sub>2</sub>SO<sub>4</sub> electrolyte solution. A saturated calomel electrode (SCE) and a platinum electrode were used as reference and counter electrode, respectively. Alternatively, a graphite rod was used as a counter electrode for stability tests. A triangular wave potential was applied on the working electrode and cyclic voltammetry data were collected in the range of −0.3 V to 0.3 V versus SCE with frequencies from 0.005 Hz to 1 Hz. The potential ranges were chosen to avoid hydrogen evolution (HER) at low potentials and the oxidation of MoS<sub>2</sub> at high potentials. The electrochemical analyses were conducted in a rectangular quartz chamber to prevent the diffraction related errors. One end of the working electrode was clamped and dipped in the electrolyte-filled rectangular chamber. The other end freely moved to perform linear actuation measurements and the bending movement was recorded by a charge coupled device (Canon 60D). Any slight change of the electrode curvature was detected at a resolution of 0.0001 mm<sup>−1</sup> curvature change with a frequency of 0.005 Hz to 30 Hz.

**Modelling.** *Multilayer bending beam model*<sup>25,32,33</sup>. Typical bending motion of a multilayer beam due to active layer expansion/contraction is shown in Extended Data Fig. 5. In what follows, we will assume that the deformation is quasi-static so that the observed macroscopic deformation can be represented by elastic strains as per the linear theory of elasticity. The lateral expansion or contraction of the active layer creates a surface stress at the interface, leading a bending deformation in the beam. The corresponding strain distribution along the bent beam cross-section varies: tensile strains at the convex surface, compressive strain at the concave surface, and zero strain at the neutral plane. The bending strain can be calculated from the normalized difference in the circumferences at a distance from the neutral plane from ref. 25:

$$\varepsilon_0(z) = \varepsilon_0 + \frac{c_z - c_0}{c_0} = \varepsilon_0 + \frac{2\pi(R+z) - 2\pi R}{2\pi R} \quad (1)$$

and

$$\varepsilon_0(z) = \varepsilon_0 + \frac{z}{R} = \varepsilon_0 + \kappa z \quad (2)$$

where  $\varepsilon_0$  is the initial strain at  $z=0$ ,  $R$  is the radius of the bent film,  $c$  is the corresponding circumference for the radius,  $\kappa$  is the bending curvature and  $z$  is the distance from the neutral plane. And the stress is given by

$$\sigma = E\varepsilon = E(\varepsilon_0 - z\kappa - \alpha) \quad (3)$$

where  $\alpha$  is the strain induced by intercalation.

The bending force ( $F$ ) and moment ( $M$ ) can be calculated by integrating the stress along the cross-section. The force and moment are given by:

$$F = \int_0^h \sigma dz = \int_0^h E(\varepsilon_0 - z\kappa - \alpha) dz \quad (4)$$

and

$$M = \int_0^h \sigma z dz = \int_0^h E(\varepsilon_0 - z\kappa - \alpha) z dz \quad (5)$$

The position of the neutral plane for multilayers depends on the mechanical and geometric properties of each layer. Therefore, the relation between curvature and induced strain is more complicated. The approach which we followed is now elaborated on.

In the equilibrium state, the total force and moment are zero for the bent beam. Considering  $\int Edz = A$ ,  $\int Ez dz = B$ ,  $\int Ez^2 dz = D$ , the force and moment can be written as:

$$A\varepsilon_0 - B\kappa = F\alpha \quad (6)$$

and

$$B\varepsilon_0 - D\kappa = M\alpha \quad (7)$$

where  $A$  is the extensional stiffness,  $B$  is bending–extension coupling stiffness and  $D$  is bending stiffness. The relation between curvature and induced strain for a multilayer beam can be obtained by integrating the force and moment equations as a function of the thickness and Young's modulus.

For a bilayer beam, the curvature is given by

$$\kappa = \frac{6m_2n_2(1+m_2)(\alpha_1 - \alpha_2)}{h_1(1+4m_2n_2+6m_2^2n_2+4m_2^3n_2+m_2^4n_2^2)} \quad (8)$$

with  $m_i = h_i/h_1$ ,  $n_i = E_i/E_1$ ,  $h$  is the layer thickness and  $E$  is the elastic modulus.

For a trilayer beam, the curvature is

$$\kappa = \frac{6(X_{12} + X_{13} + X_{23})}{h_1(1+Y_2+Y_3+Y_{23})} \quad (9)$$

where

$$X_{12} = m_2n_2(1+m_2)(\alpha_1 - \alpha_2) \quad (10)$$

$$X_{13} = m_3n_3(1+2m_2+m_3)(\alpha_1 - \alpha_3) \quad (11)$$

$$X_{23} = m_2n_2m_3n_3(m_2+m_3)(\alpha_2 - \alpha_3) \quad (12)$$

and

$$Y_2 = 4m_2n_2 + 6m_2^2n_2 + 4m_2^3n_2 + m_2^4n_2^2 \quad (13)$$

$$Y_3 = 4m_3n_3 + 6m_3^2n_3 + 4m_3^3n_3 + m_3^4n_3^2 \quad (14)$$

$$Y_{23} = m_2m_3n_3[(4m_2^2+6m_2m_3+4m_3^2)n_2+12(1+m_2+m_3)] \quad (15)$$

Since only one active layer contributes to actuation, the curvature for a three-layer electrochemical actuator can be represented as:

$$\kappa = \frac{-6m_3n_3[1+2m_2+m_3+m_2n_2(m_2+m_3)]}{h_1(1+Y_2+Y_3+Y_{23})} \alpha_3 \quad (16)$$

As in all previous analyses reported in the literature<sup>25</sup>, the model we used assumes no appreciable space charge at the interface of the electrode and the electroactive layer. Since the model was used to compare the performance of the actuators with each other on a relative basis, this assumption has no impact on the evaluation or assessment of actuator performance.

*The Stoney model.* The thin film approximation<sup>34,35</sup> first assumes that the substrate is appreciably thicker than the film ( $t_1 \gg t_2$ ), which ensures that the film is under a plane-stress state of stress (2D). In other words, the out-of-plane normal stress is zero as there are no traction forces on the surface of the film. However, the state of strain in the film is still 3D. Also, the thicknesses of each layer are assumed to be much smaller than the lateral dimensions. Second, the material is homogenous, isotropic, and linearly elastic. Third, all shear stresses and strain are assumed to vanish, making the Cartesian coordinate system fundamentally the so-called principal axes. Finally, rotations and strains are infinitely small. Here, in-plane strain ( $\varepsilon_{\parallel}$ ) is related to the out-of-plane strain ( $\varepsilon_{\perp}$ ) via  $\nu\varepsilon_{\perp} = -\varepsilon_{\parallel}$ , where  $\nu$  is the Poisson's ratio, and is given by  $\nu \approx -0.5(E_{\perp}/E_{\parallel})$  with  $E_{\parallel}$  and  $E_{\perp}$  the elastic in-plane and out-of-plane elastic moduli, respectively. It follows from the Hooke's law that the stress in the film is related to the strain via

$$\sigma_1 \approx E_1' \Delta \varepsilon_0 \quad (17)$$

where  $\Delta \varepsilon_0$  is the strain induced by the substrate. The curvature of a freely bent bilayer film can be expressed with strain mismatch as

$$K = \frac{6E_2't_2}{E_1't_1^2} \Delta \varepsilon_0 \quad (18)$$

Then the residual force can be calculated with the Stoney approach by neglecting the thinner layer,

$$\sigma_{S1} = \frac{E_1't_1^2}{6t_2} K \quad (19)$$

where  $E_1'$  is the biaxial modulus of the first layer,  $\sigma_{S1}$  is the interfacial stress,  $t_1$  and  $t_2$  are thicknesses of each layer, and  $K$  is the curvature.

*Work density calculations.* The volumetric ( $W_v$ ) and gravimetric ( $W_g$ ) work densities of single layer and free restacked 1T MoS<sub>2</sub> film were calculated using<sup>1</sup>;

$$W_v = \frac{E\varepsilon^2}{2} \quad (20)$$

$$W_g = \frac{E\varepsilon^2}{2\rho} \quad (21)$$

In constrained systems such as a bilayer beam, the active material cannot freely strain under the imposed state of stress (plane stress). The interfacial traction creates a bending moment that deflects the beam. Then, the work ( $W$ ) in the bending beam is determined by the product of bending moment  $M$  and the bending angle  $\theta$ , which can be obtained from the bending curvature and the actuator length<sup>25</sup>. The curvature can be represented by the ratio of bending moment ( $M$ ) to bending stiffness ( $EI$ ) according to Euler beam theory via

$$W = \frac{M\theta}{2} = \frac{M\kappa L}{2} \quad (22)$$

with

$$\kappa = \frac{M}{EI} \quad (23)$$

resulting in

$$W = \frac{M^2 L}{2EI} \quad (24)$$

By integrating previously constructed moment values for a multilayer actuator, the moment is

$$M = \frac{E_1 b h_1^3 (1 + Y_2 + Y_3 + Y_{23})}{2} \times (\alpha_1 + (m_2^2 + 2m_2)n_2\alpha_2 + (m_2^2 + 2m_3(1 + m_2))n_3\alpha_3) \quad (25)$$

and the bending stiffness is

$$EI = \frac{E_1 b h_1^3 (1 + Y_2 + Y_3 + Y_{23})}{12(1 + m_2 n_2 + m_3 n_3)} \quad (26)$$

*Calculation of gravimetric and volumetric capacitances of the electrode.* The specific capacitances were calculated from cyclic voltammetry plots using the following equations:

$$C_g = \frac{\int IdV}{vmV} \quad (27)$$

$$C_v = C_g \rho \quad (28)$$

where  $C_g$  is the gravimetric capacitance ( $F g^{-1}$ ),  $C_v$  is the volumetric capacitance ( $F cm^{-3}$ ),  $v$  is the scan rate ( $V s^{-1}$ ),  $m$  is the mass (g),  $V$  is the potential range, and  $\rho$  ( $g cm^{-3}$ ) is the density of restacked MoS<sub>2</sub>. The density ( $g cm^{-3}$ ) of restacked MoS<sub>2</sub> was determined from the weight of the electrode and the volume of the MoS<sub>2</sub> films.

The energy density and power density of the metallic MoS<sub>2</sub> electrodes were calculated according to the following equations:

$$E = \frac{0.5 C_T \Delta V^2}{3,600} \quad (29)$$

$$E_v = E \rho \quad (30)$$

$$P = \frac{E \times 3,600}{t_{\text{discharge}}} \quad (31)$$

$$P_v = P \rho \quad (32)$$

where  $C_T$  is the total capacitance of the two-electrode cell,  $\Delta V$  is the effective potential range during the discharging process,  $t_{\text{discharge}}$  is the discharging time (s),  $\rho$  is the density of the electrode,  $E$  is the gravimetric energy density ( $W h g^{-1}$ ),  $E_v$  is the volumetric energy density in  $W h cm^{-3}$ ,  $P$  is the gravimetric power density ( $W g^{-1}$ ), and  $P_v$  is the volumetric power density in  $W cm^{-3}$ .

*Inverted S-beam calculations.* When the mass was hung on it, the ISC actuator stretched vertically, similarly to a spring where the displacement is proportional to the applied force, as shown in Extended Data Fig. 6. In this configuration, the system is subjected to gravitational forces, buoyancy, spring force and friction force. At equilibrium, these forces balance out and any additional force will disturb the equilibrium until it reaches the new equilibrium state. Gravitational force and buoyancy were calculated from the mass and volume of the hung weight. These forces were balanced by the spring force and the spring constant was derived from the displacement.

The spring force ( $F$ ) is given by

$$F = -kx \quad (33)$$

whereas the work is given by

$$W = \int F(x) dx \quad (34)$$

The ISC actuator was electrochemically actuated without the mass, and a reversible actuation was observed with 5.5 mm displacement. The corresponding electrochemically induced force and work were calculated by using the spring constant. Then the mass-loaded ISC actuator was electrochemically driven, and the corresponding force and work were calculated.

The electromechanical coupling factor ( $k^2$ ) is the ratio of mechanical work to stored energy density<sup>1</sup> which is given by:

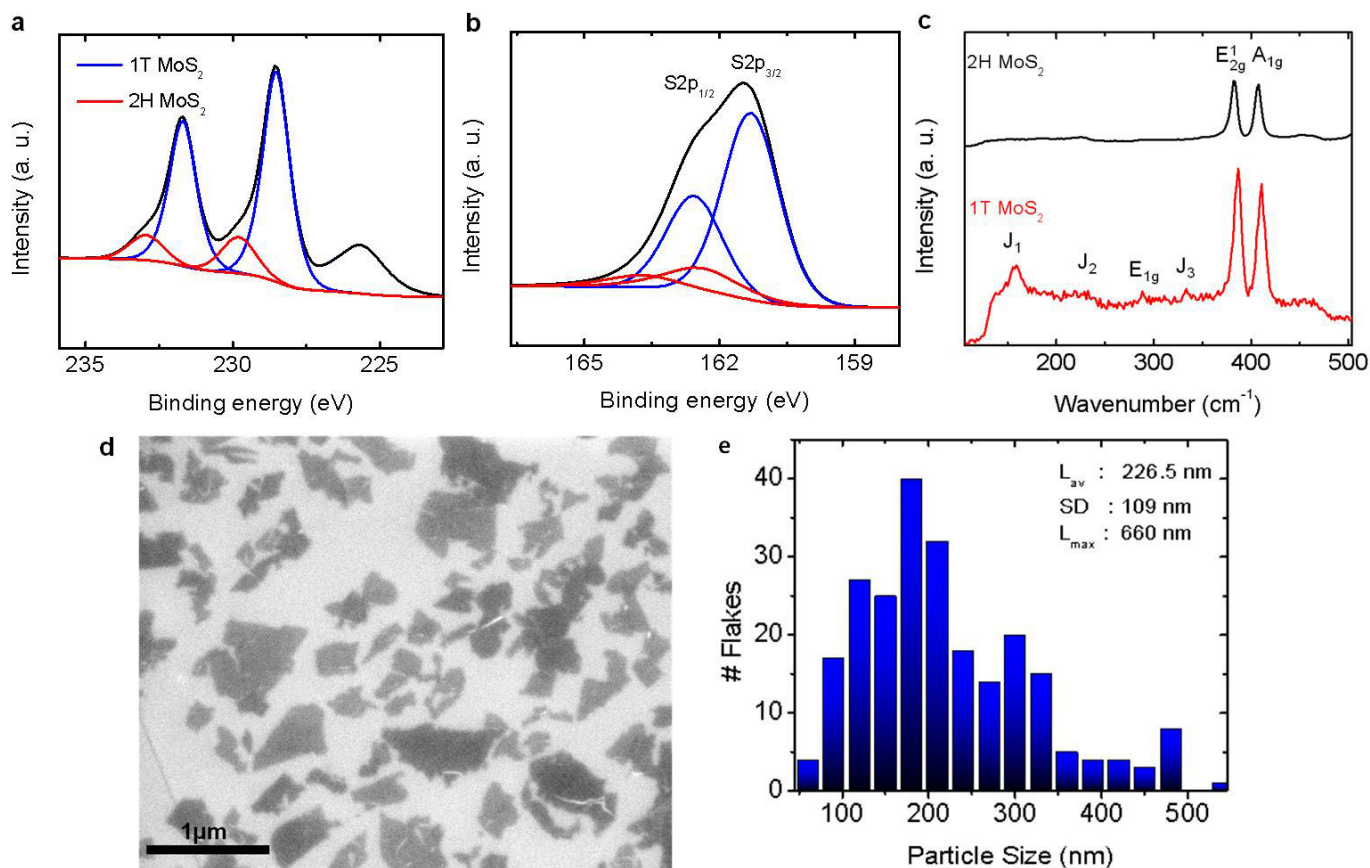
$$k^2 = \frac{\frac{1}{2} E \varepsilon^2 V^2}{\frac{1}{2} C V^2 \rho} \quad (35)$$

We used the above equation for assessing the electromechanical energy conversion of the actuators. By dividing the generated mechanical work by the stored energy, the electromechanical coupling factors ( $k^2$ ) were calculated and were found to be 0.5–0.6.

*Nanoindentation.* We measured the modulus of 3- $\mu$ m and 8- $\mu$ m MoS<sub>2</sub> films by nanoindentation in dry, wet and charging/discharging conditions, and found the modulus to be comparable to or higher than what we measured by beam bending. We made hundreds of measurements and thus values represent the average values.

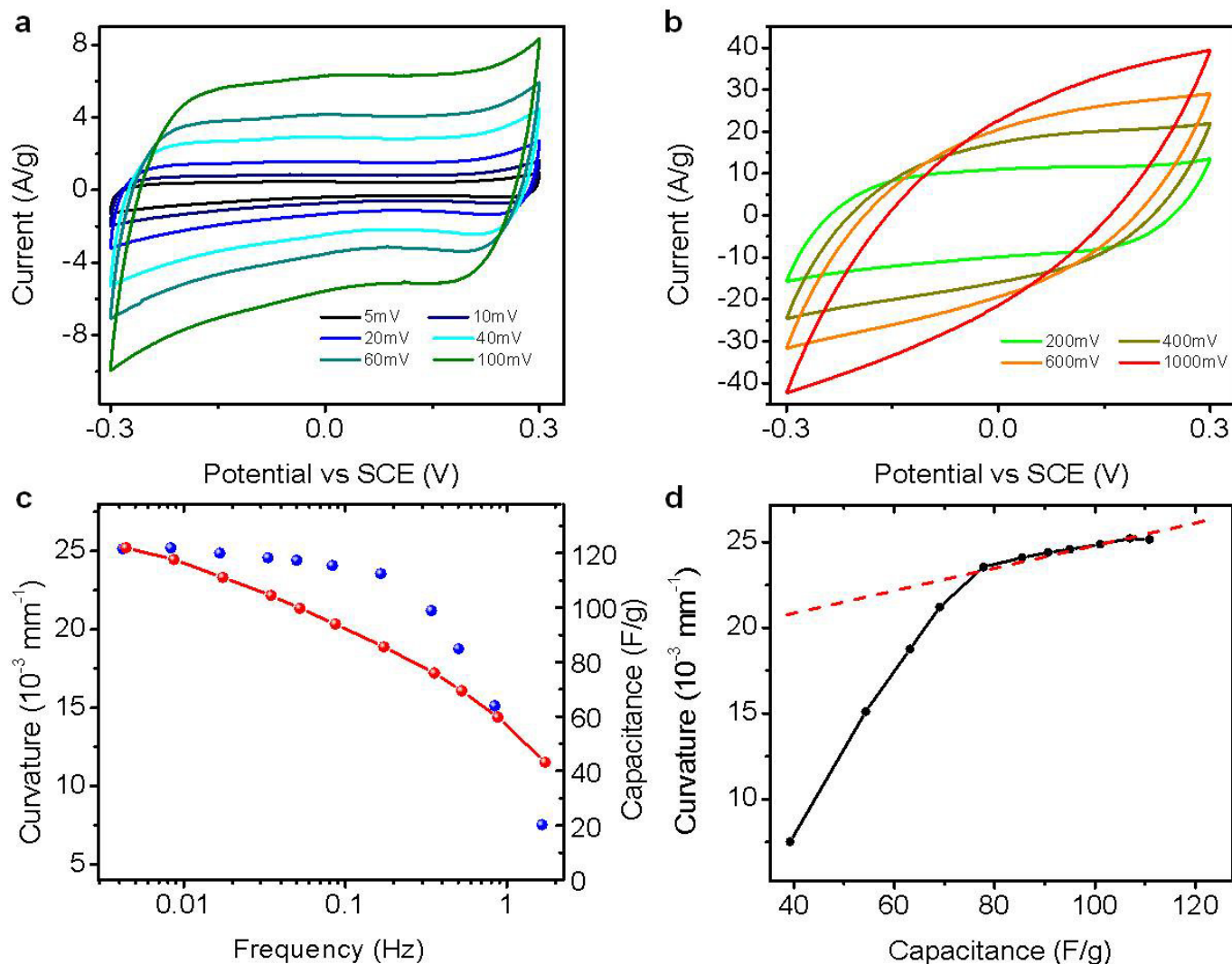
**Data availability.** The data that support the findings of this study are available from the corresponding author upon reasonable request.

31. Eda, G. *et al.* Photoluminescence from chemically exfoliated MoS<sub>2</sub>. *Nano Lett.* **11**, 5111–5116 (2011).
32. Timoshenko, S. & Goodier, J. N. *Theory of Elasticity* (McGraw-Hill, 1951)
33. Sokolnikoff, I. S. *Mathematical Theory of Elasticity* (McGraw-Hill, 1946).
34. Klein, C. A. How accurate are Stoney's equation and recent modifications. *J. Appl. Phys.* **88**, 5487 (2000).
35. Stoney, G. G. The tension of metallic films deposited by electrolysis. *Proc. R. Soc. Lond. A* **82**, 172–175 (1909).
36. Pelrine, R. High-speed electrically actuated elastomers with strain greater than 100%. *Science* **287**, 836–839 (2000).
37. Haines, C. S. *et al.* Artificial muscles from fishing line and sewing thread. *Science* **343**, 868–872 (2014).
38. Hara, S., Zama, T., Takashima, W. & Kaneto, K. Artificial muscles based on polypyrrole actuators with large strain and stress induced electrically. *Polym. J.* **36**, 151–161 (2004).
39. Foroughi, J. *et al.* Torsional carbon nanotube artificial muscles. *Science* **334**, 494–497 (2011).
40. Mirfakhrai, T. *et al.* Electrochemical actuation of carbon nanotube yarns. *Smart Mater. Struct.* **16**, S243–S249 (2007).
41. Xie, X., Bai, H., Shi, G. & Qu, L. Load-tolerant, highly strain-responsive graphene sheets. *J. Mater. Chem.* **21**, 2057 (2011).
42. Jiménez Sandoval, S., Yang, D., Frindt, R. & Irwin, J. Raman study and lattice dynamics of single molecular layers of MoS<sub>2</sub>. *Phys. Rev. B* **44**, 3955–3962 (1991).
43. Calandra, M. Chemically exfoliated single-layer MoS<sub>2</sub>: stability, lattice dynamics, and catalytic adsorption from first principles. *Phys. Rev. B* **88**, 245428 (2013).



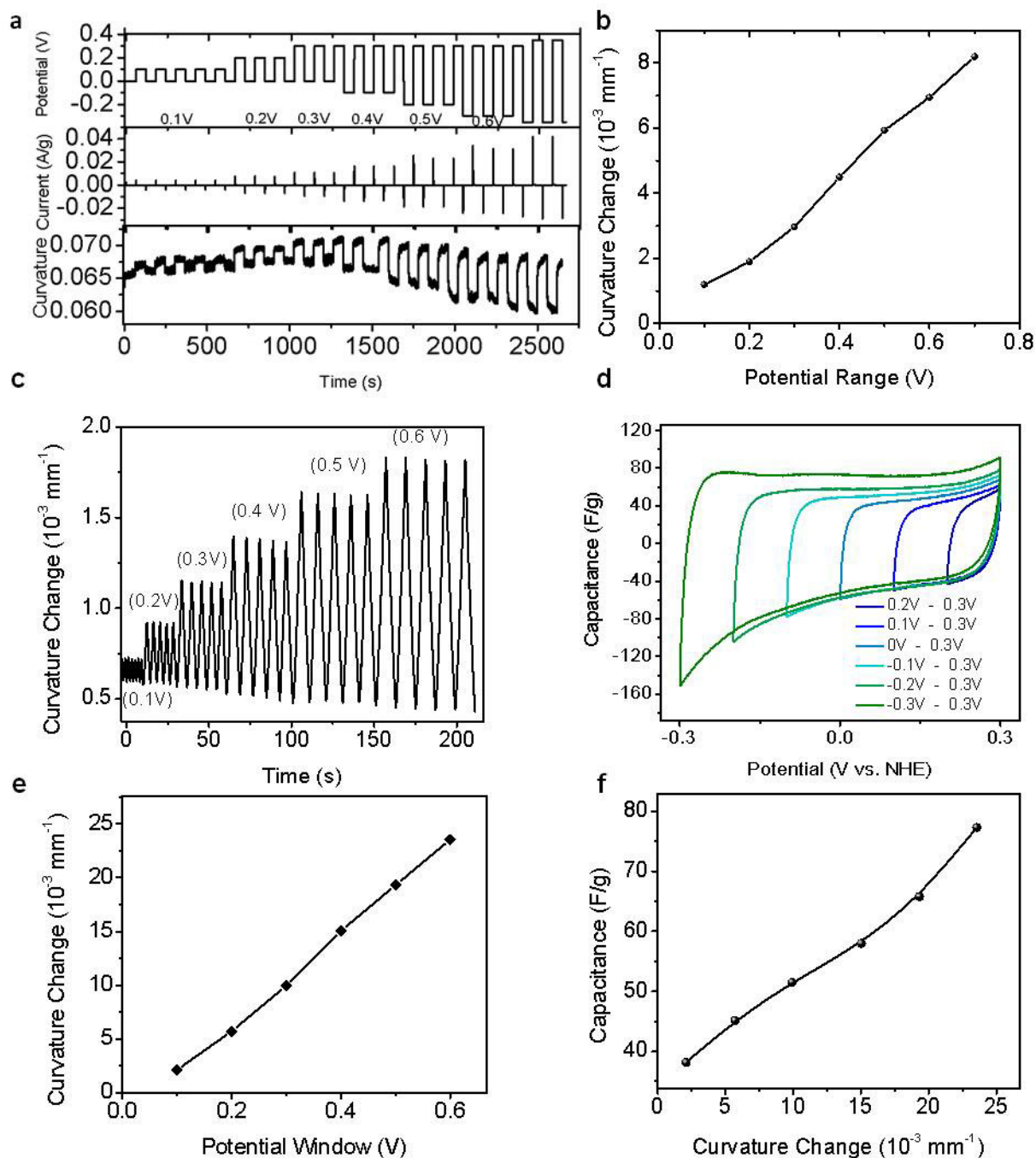
**Extended Data Figure 1 | Structural characterization of 1T phase MoS<sub>2</sub> nanosheets.** **a, b**, High-resolution X-ray photoelectron spectrum from the Mo 3*d* region (**a**) and the S 2*p* region (**b**) of as-exfoliated 1T MoS<sub>2</sub> film. Spectra from 1T and 2H phases are indicated as blue and red curves, respectively. **c**, 1T phase MoS<sub>2</sub> has distinctive Raman peaks (J<sub>1</sub>, J<sub>2</sub> and J<sub>3</sub> peaks at 156 cm<sup>-1</sup>, 226 cm<sup>-1</sup> and 333 cm<sup>-1</sup>, respectively) in addition to two main Raman modes—the in-plane mode E<sub>2g</sub><sup>1</sup>, and the out-of-plane mode,

A<sub>1g</sub> (refs 42, 43). The 1T phase of MoS<sub>2</sub> was identified from the presence of E<sub>1g</sub><sup>1</sup>, J<sub>1</sub>, J<sub>2</sub> and J<sub>3</sub> peaks. **d, e**, The MoS<sub>2</sub> flake size analyses were conducted by counting the individual flakes in multiple SEM images (example in **d**). The size of the exfoliated monolayer MoS<sub>2</sub> flakes varies from 50 nm to 700 nm; the average flake size is 226.5 nm with 109 nm standard deviation (**e**).



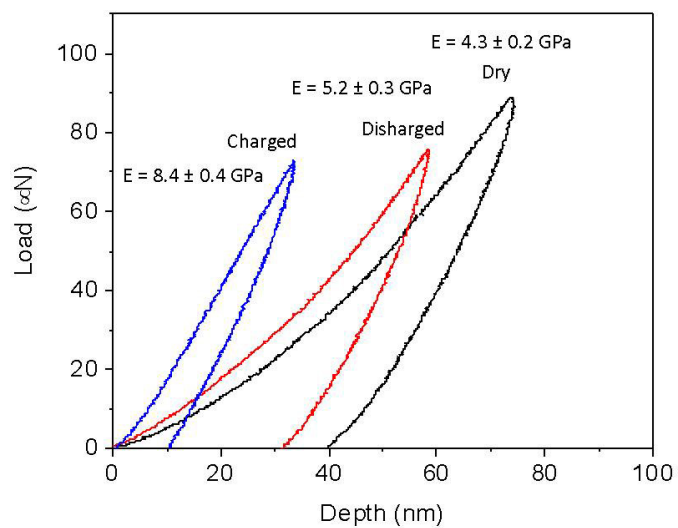
**Extended Data Figure 2 | Relationship between capacitance and curvature.** **a, b**, Current–voltage curves at different scan rates (see keys) for 1T phase  $\text{MoS}_2$  film electrodes. The similarity in behaviour at different scan rates indicates that charging and discharging can be done slowly or rapidly, allowing stable actuation at varying frequencies. SCE, standard calomel electrode. **c, d**, Variation of electrochemical actuation

and capacitance with frequency. **c**, Curvature change (blue points) and capacitance (red points) as a function of frequency. **d**, Curvature versus capacitance (data points); the dashed line represents a linear fit at low scan rates. The deviation from this line represents the influence of drag forces from the liquid.

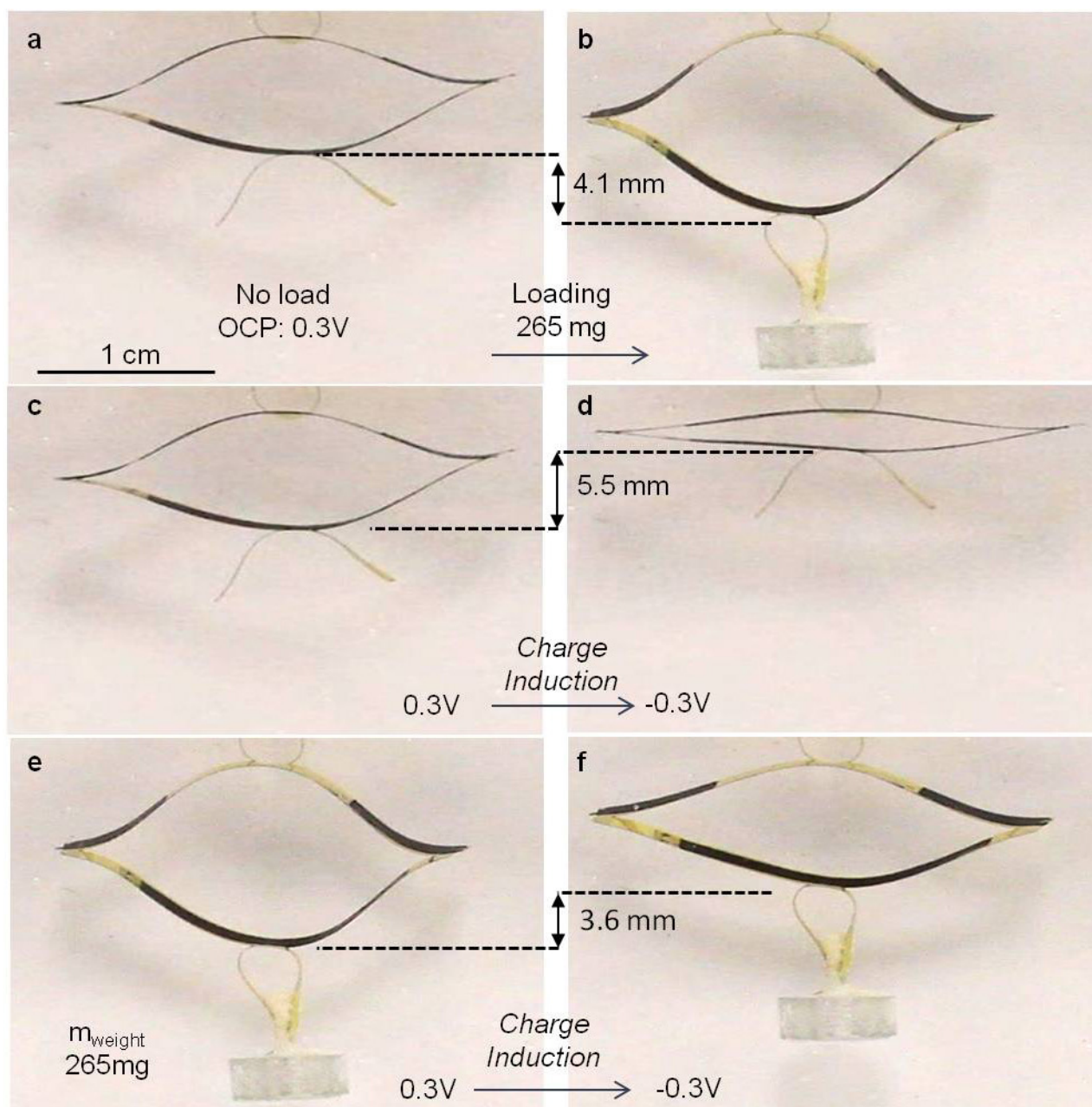


**Extended Data Figure 3 | Influence of electrochemical parameters on curvature.** **a**, Variation of electrochemical actuation and capacitance with applied potential. **b**, Curvature change induced by square wave potentials over different potential ranges. **c**, The curvature change induced by triangular wave potentials; the curvature response to triangular potentials

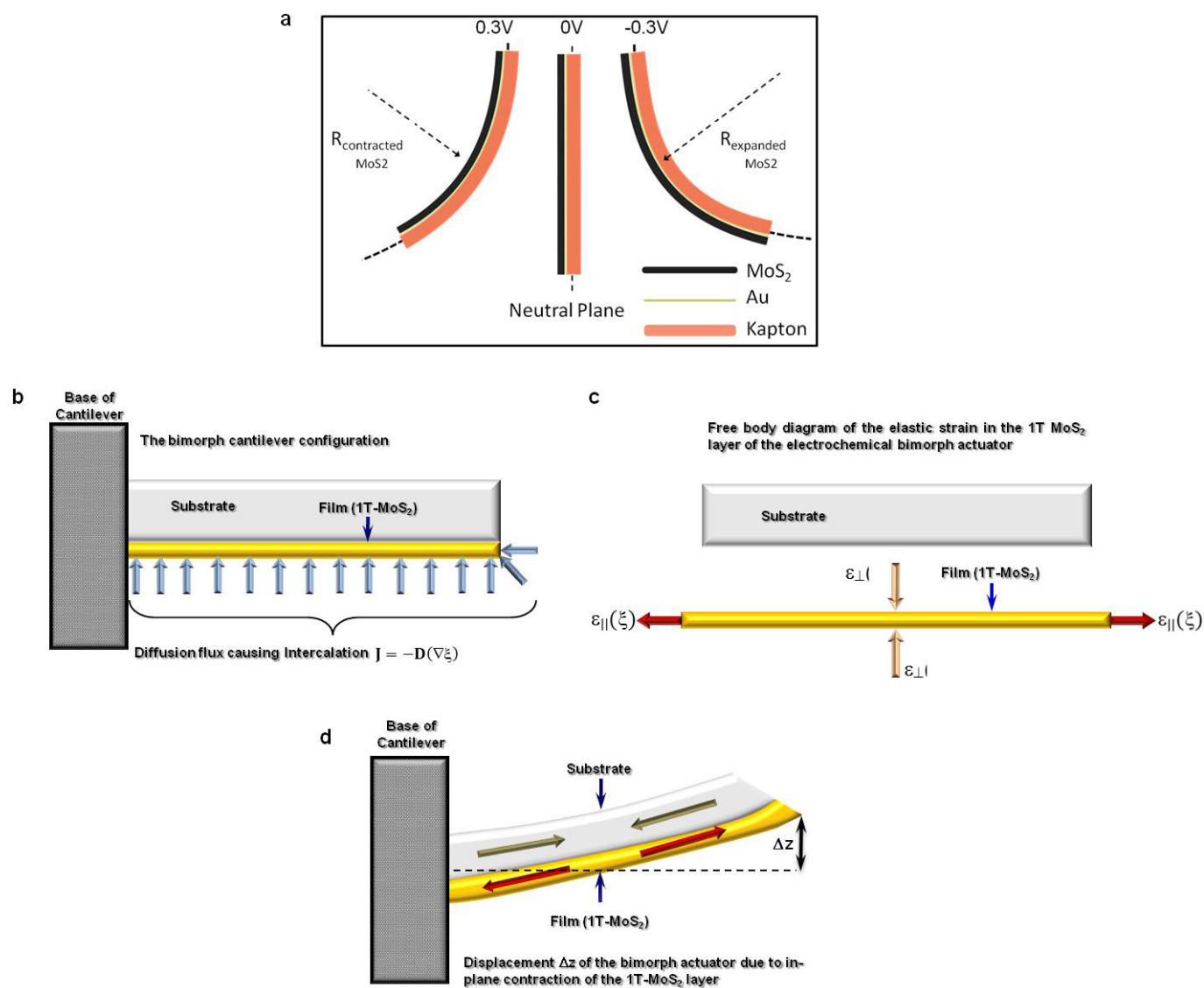
at voltages from 0.1 V to 0.6 V is shown. **d**, Capacitance–voltage curves with expanding electrochemical potential window (key). **e**, Curvature as a function of electrochemical potential. **f**, Capacitance versus curvature change.



**Extended Data Figure 4 | Typical nanoindentation loading versus depth traces for 8- $\mu\text{m}$ -thick  $\text{MoS}_2$  film.** The elastic modulus values ( $E$ ) of dry, charged and discharged states of the film are shown. Results for the 3- $\mu\text{m}$ -thick films were similar to those of the 8- $\mu\text{m}$ -thick films.



**Extended Data Figure 5 | Photographs of the ISC actuator device at different states of induction.** a, b, The displacement of the ISC actuator (4.1 mm) under loading of 265 mg. c–f, Also shown is the displacement (5.5 mm) via electrochemical induction (0.3 to –0.3 V) without the load (c, d), and the displacement (3.6 mm) via the same electrochemical induction with the load (265 mg; e, f).



**Extended Data Figure 6 | Diagrams showing beam-bending modelling of the actuation behaviour.** **a**, Schematic summarizing the bending behaviour of the 1T-MoS<sub>2</sub>-based bimorph actuator as a function of voltage polarity. **b**, Cantilever actuator configuration representing the mechanics of electrochemical actuation due to the diffusion flux ( $J$ ) of intercalating species into the 1T MoS<sub>2</sub> film of the bimorph structure under isothermal conditions. The constant temperature makes constant the diffusivity ( $D$ ) of the intercalating species in 1T MoS<sub>2</sub>. Here, the ingress of the intercalating species is through all surfaces that are exposed to the liquid medium. The driving force for the ingress is the concentration gradient of the intercalating species ( $\nabla\xi$ ) that is formed between the 1T MoS<sub>2</sub>-liquid interface and the interior of the 1T MoS<sub>2</sub> film. **c**, Free body diagram of the bimorph showing the elastic (recoverable) strains developed in the 1T MoS<sub>2</sub> film due to the intercalation process. The intercalating species cause the 1T MoS<sub>2</sub> film to contract in the direction perpendicular to the normal surface of the film, resulting in a compressive out-of-plane strain  $\varepsilon_{\perp}$ . The compressive  $\varepsilon_{\perp}$  induces an in-plane expansion as represented by the

tensile in-plane strain  $\varepsilon_{\parallel}$ . The in-plane and out-of-plane strains are related via  $\varepsilon_{\perp} = -2(E_{\parallel}/E_{\perp})\varepsilon_{\parallel}$  due to the plane state of stress<sup>32,33</sup>, where  $E_{\parallel}$  and  $E_{\perp}$  are the in-plane and out-of-plane elastic moduli, respectively. The  $(\varepsilon_{\parallel}/\varepsilon_{\perp})$  ratio represents the Poisson's ratio. The normal in-plane strains are assumed to be isotropic, while the in-plane shear strain is presumed to be completely relieved: both these are a consequence of the in-plane rotation of 1T MoS<sub>2</sub> nanosheets comprising the film being random around the normal axis, that is, the existence of mosaic structure. **d**, The resultant deformation of the cantilever bimorph actuator. The tensile in-plane strain  $\varepsilon_{\parallel}$  in the 1T MoS<sub>2</sub> film induces deformation in the substrate due to traction at the film-substrate interface, that is, clamping of the electrochemically active film by the substrate. The consequence is a tip displacement ( $\Delta z$ ) of the bimorph actuator (the system) that does work on the surroundings (the inertial weight). The inverse bell-shaped bimorph actuator (see Extended Data Fig. 6) can be thought of as back-to-back bimorph cantilever actuators that are 'welded' at the tips where maximum ( $\Delta z_{\text{max}}$ ) deflection occurs.

Extended Data Table 1 | Literature survey of actuator performance

Type of Actuator	Type of Stimulus	Strain (%)	Stress (MPa)	Working Frequency	Potential Window	Advantages	Disadvantages	References
Piezoelectric ceramic (PZT)	Piezoelectric	0.2	110	Fast (kHz)	High (kV)	Fast response High generative force Wide bandwidth	High electric field Low strain Brittle	Pelrine, Mat.Sc. Eng, 2000
Piezoelectric polymer (PVDF)	Piezoelectric	0.1	4.8	Fast (kHz)	High (kV)	Fast response Wide bandwidth	Flexible Low mechanical output High electric field	Pelrine, Mat.Sc. Eng, 2000
Electrostrictive polymer (PVDF-TrFE)	Electrostrictive	4.3	43	Fast (kHz)	High (kV)	Fast response Flexible High stress generation	Operates above Curie Temp. High electric field	Zhang, Science, 1998 Brochu, Adv. Mat. 2010
Dielectric elastomer (Acrylic with pre-strain)	Electrostrictive	215	2.4	Fast (kHz)	High (kV)	Very large stroke Light weight Low cost, stability	Defect sensitive, Poor mechanics (viscoelastic) Leakage current	Pelrine, Science, 2000
Shape Memory Alloy (Ti-Ni)	Phase transformation	5	200	Slow	Temperature gradient (0-135°C)	High work density	Slow Low efficiency	Pelrine, Mat.Sc. Eng, 2000
Natural muscle (human skeletal)	Biochemical	40	0.35	Moderate	--	High stroke Self healing	Limited stress generation	Brochu, Adv. Mat. 2010
Carbon nanotubes (CNTs)	Thermal expansion	1.5	16	Slow	Temperature gradient (0-2500°C)	High stroke High stress	High operating temperature Passive cooling	Lima, Science, 2012
Nylon (6,6)	Thermal expansion	10	22	Moderate (5 Hz)	Temperature gradient (0-240°C)	High stroke	Need additional unit for heating/cooling	Haines, Science, 2014
Conjugated polymer (PEE-Ppy)	Solvent sorption	--	27	Moderate (0.3 Hz)	Concentration gradient	High stroke	Require ambient water gradient	Ma, Science, 2013
Conductive polymers (PPy)	Electrochemical (Redox)	7	5	Low (0.01Hz)	1.6 V	Biocompatible Soft Low potential	Low mechanical strength	Hara, Polymer J. 2004
CNT yarns	Electrochemical (Double layer charge injection)	Torsional 0.8 (Preload) 0.12	No load Preload 50	Moderate (0.1-0.5Hz)	4 V	High stroke Withstand high loading	Useful for rotating systems, Creep	Foroughi, Science, 2011 Mirfakhrai, Smart Mat. & Str., 2007
CNT/PANy	Electrochemical (Redox)	0.85 (Preload) 0.7	No load Preload 25 Mpa	Low (0.0035Hz)	0.7 V	Withstand high loading High work-per-cycle	Slow response (High frequency is not reported)	Spinks, Adv. Materials 2006
Graphene	Electrochemical (Double layer charge injection)	0.85	6.1	Low (0.002 Hz)	2.4 V	Large curvature change	Slow response (Strain is 0.35 at 0.02Hz)	Xie, J.Mat.Chem., 2010
Nanoporous metals (Au-Pt)	Electrochemical (Adsorption)	3.9	--	Very low (0.00025Hz)	1.6 V	High elastic energy density	Slow response Expensive Microscale	Jin, Nanoletters, 2010
Transition metal oxides (V2O5)	Electrochemical (Redox)	0.21	5.9	Low (0.005Hz)	2 V	Redox active Abundant	Slow response Require orientation	Gu, Nature, 2003
HOPG	Electrochemical (Solid-state intercalation)	6.7 1.3	10 100	Very low (10 <sup>-6</sup> Hz)	1V	High energy density	Very slow response Safety issues due to Li	Koyama, Adv. Func. Mat., 2006 Chin, ECS Solid State Let., 2006
MoS <sub>2</sub> (Current study)	Electrochemical (Intercalation Redox)	0.8 0.5	17 11	0.0042 Hz 0.125 Hz	0.6 V	High displacement High generated force Low potential	Tendency to delaminate under high load	--

Comparison of the performance of different actuator materials with different types of actuation stimuli<sup>2-4,9,36,37</sup>, including electrochemical induction<sup>11,15,16,18,20,38-41</sup>. Frequency values of electrochemical actuators were compared where the highest strain was observed. The typical convention used to define the frequency intervals for actuators depends on the actuator type. For instance, piezoelectric-based electromechanical actuators that operate near a fundamental mode of resonance are typically considered low frequency for <100 kHz, intermediate frequency for about 400–500 kHz, and high frequency for >10 MHz. For electrochemical actuators, which operate quasi-statically, we consider 1–100 Hz as high, 0.1–1 Hz as moderate and <0.1 Hz as low frequency. The work frequency refers to the frequency at which highest strain is observed.